

# Red-phosphorus-impregnated carbon nanofibers for sodium-ion batteries and liquefaction of red phosphorus

Yihang Liu <sup>1✉</sup>, Qingzhou Liu<sup>2</sup>, Cheng Jian<sup>3</sup>, Dingzhou Cui<sup>1</sup>, Mingrui Chen<sup>2</sup>, Zhen Li<sup>2</sup>, Teng Li <sup>3</sup>, Tom Nilges<sup>4</sup>, Kai He <sup>5✉</sup>, Zheng Jia <sup>6✉</sup> & Chongwu Zhou<sup>1,2✉</sup>

Red phosphorus offers a high theoretical sodium capacity and has been considered as a candidate anode for sodium-ion batteries. Similar to silicon anodes for lithium-ion batteries, the electrochemical performance of red phosphorus is plagued by the large volume variation upon sodiation. Here we perform in situ transmission electron microscopy analysis of the synthesized red-phosphorus-impregnated carbon nanofibers with the corresponding chemo-mechanical simulation, revealing that, the sodiated red phosphorus becomes softened with a “liquid-like” mechanical behaviour and gains superior malleability and deformability against pulverization. The encapsulation strategy of the synthesized red-phosphorus-impregnated carbon nanofibers has been proven to be an effective method to minimize the side reactions of red phosphorus in sodium-ion batteries, demonstrating stable electrochemical cycling. Our study provides a valid guide towards high-performance red-phosphorus-based anodes for sodium-ion batteries.

<sup>1</sup>Department of Electrical Engineering, University of Southern California, Los Angeles, California 90089, USA. <sup>2</sup>Department of Materials Science and Engineering, University of Southern California, Los Angeles, California 90089, USA. <sup>3</sup>Department of Mechanical Engineering, University of Maryland, College Park, Maryland 20742, USA. <sup>4</sup>Department of Chemistry, Technical University of Munich, 85748 Garching b. München, Germany. <sup>5</sup>Department of Materials Science and Engineering, Clemson University, Clemson, South Carolina 29634, USA. <sup>6</sup>Department of Engineering Mechanics, Zhejiang University, Hang Zhou, Zhejiang 310058, China. ✉email: [yihangl@usc.edu](mailto:yihangl@usc.edu); [kaihe@clemson.edu](mailto:kaihe@clemson.edu); [zheng.jia@zju.edu.cn](mailto:zheng.jia@zju.edu.cn); [chongwuz@usc.edu](mailto:chongwuz@usc.edu)

Lithium-ion chemistry has been extensively implemented to store energy and deliver power for cellular and automotive applications, owing to its remarkably high energy density and long cycle life<sup>1–3</sup>. However, the potential environmental impacts and the unevenly distributed lithium deposits have sparked an exploration of alternative energy storage strategies, such as sodium-ion chemistry<sup>4–8</sup>. The anode part has been considered as the major stumbling block of sodium-ion chemistry because the intercalation of Na ions into graphite is thermodynamically unfavourable; this problem is intuitively associated with the larger ionic radius of the sodium ions, while the reaction energetics may also play a more deterministic role since larger alkali metal ions can exhibit reversible intercalation<sup>6</sup>. Nevertheless, it implies that we should not simply adopt the recent strategies for lithium-ion battery electrode materials directly to sodium-ion chemistry. The commercialization of sodium-ion batteries demands appropriate options of anode materials. Phosphorus (P) is one of the most abundant elements in the continental crust and oceans, and its specific capacity of 2596 mAh g<sup>-1</sup> offers much promise to sodium-ion batteries. The white phosphorus (P<sub>white</sub>) is extremely toxic and reactive, and the production method of black phosphorus (P<sub>black</sub>) is costly and poorly scalable, promoting red phosphorus (P<sub>red</sub>) into a better position for sodium-ion storage<sup>9,10</sup>.

Just like silicon anodes for lithium-ion batteries, P<sub>red</sub> anode was believed to be suffering from its insulating nature and huge volumetric expansion upon ion intercalation. Borrowing the ideas from the significantly improved performance of silicon anodes during the past two decades, P<sub>red</sub> was usually bundled with conductive scaffold, such as carbon nanotubes<sup>11–13</sup>, graphene<sup>14–16</sup>, and other carbonaceous materials<sup>17–21</sup> to solve the above issues; and thus many researchers, including us, assumed that P<sub>red</sub> would have the same major problems as silicon: >300% volume expansion from P<sub>red</sub> to Na<sub>3</sub>P would cause severe pulverization of the particles and lead to the loss of active material. Although the electrochemical performance of P<sub>red</sub> has been greatly improved, evidence revealing the fundamental mechanism of its capacity decay is still unclear and the long-term cycling performance remains unsatisfied.

To investigate the sodiation process and the capacity decay mechanism of P<sub>red</sub>, we synthesize P<sub>red</sub>-impregnated carbon nanofiber composite (P<sub>red</sub>@CNF), whose one-dimensional structure makes it ideal to observe the sodiation behaviour of P<sub>red</sub>, and the highly conductive CNF shell can serve as electron pathway to improve the charge transfer kinetics of P<sub>red</sub>. Our in situ transmission electron microscopy (TEM) analysis on the sodiation process of P<sub>red</sub>@CNF reveals that P<sub>red</sub> particles become softened during the sodiation process with a “liquid-like” mechanical property, and the corresponding chemo-mechanical simulation indicates that P<sub>red</sub> should suffer much less from the volume variation and fracture than the silicon anodes in lithium-ion chemistry. Based on the above observation and simulation, we conclude that the main cause of the P<sub>red</sub> capacity degradation should be the side reactions that occur during the formation of highly reactive sodiated phosphorus compounds. Furthermore, the designed encapsulation strategy of the synthesized P<sub>red</sub>@CNF composite has been proven to be an effective route to avoid the unfavourable side reactions of P<sub>red</sub> anode during long-term cycling: the P<sub>red</sub>@CNF anode can deliver ~1850 mAh g<sup>-1</sup> specific capacities over 500 cycles at 0.1 A g<sup>-1</sup> current density, and >1000 mAh g<sup>-1</sup> capacity over 5000 cycles at 1 A g<sup>-1</sup> rate.

## Results

**As-synthesized material structures.** P<sub>red</sub>@CNF was synthesized through the vaporization–condensation method. First, P<sub>red</sub> was deposited onto and into the CNFs in a sealed quartz ampoule

under vacuum, and then the exceeding P<sub>red</sub> coated outside of the CNFs was removed with a flash-heat process in an argon-flowed tube furnace, as described in the Methods section and the process flow in Supplementary Fig. 1a. The scanning electron microscopy (SEM) image of the P<sub>red</sub>@CNF composite is exhibited alongside the energy-dispersive analytical X-ray spectroscopy (EDS) profile of phosphorus elemental distribution in Fig. 1a and 1b, where CNFs can be visualized under SEM, and the elemental mapping profile of phosphorus is in a good agreement with the CNF morphology, indicating that most of the phosphorus has been confined inside CNFs. The TEM (Fig. 1c), corresponding high-angle annular dark-field scanning transmission electron microscopy (HAADF-STEM; Fig. 1d), and the EDS mapping images (Fig. 1e) show that the diameter of CNFs is ~100 nm, and the P<sub>red</sub> segments were encapsulated in CNFs, forming the core-shell nanostructure. The highly graphitized CNF shell provides excellent electronic conductivities and thus improves the charge transfer of P<sub>red</sub> segments, and the free space between P<sub>red</sub> segments can further accommodate the substantial volume expansion. Additional SEM and TEM characterization at different synthesis stages can be found in Supplementary Fig. 1b–j. In Supplementary Fig. 1h and 1i, the P<sub>red</sub> segments and the core-shell nanostructure can be visualized in most of the CNFs under SEM at an acceleration voltage of 15 kV, indicative of the good uniformity of synthesized P<sub>red</sub>@CNF sample. The Raman spectra of the P<sub>red</sub>@CNF composite is exhibited in Fig. 1f, where the P<sub>red</sub> band ranging from 300 to 500 cm<sup>-1</sup> is observed, and the characteristic peaks of CNF such as D, G, and G' bands can be identified<sup>22,23</sup>. In both Raman (Fig. 1f) and X-ray photoelectron spectroscopy (XPS) results (Supplementary Fig. 2a), no obvious P–C bond signal can be detected<sup>24</sup>, and the carbon 1s XPS profiles of pristine CNF and synthesized P<sub>red</sub>@CNF are almost identical, indicating that the bond structure is not significantly affected by the heat treatment process. In the XPS profile of phosphorus 2p edge (Supplementary Fig. 2b), a small P–O bond peak can be attributed to air exposure during the sample transfer process. The Fourier-transform infrared spectroscopy (FTIR) profiles of CNF, P<sub>red</sub>, and the as-prepared P<sub>red</sub>@CNF are exhibited in Supplementary Fig. 3, where the P=O bond signal can be detected from both P<sub>red</sub> and P<sub>red</sub>@CNF samples; however, no obvious P–O–C or P–C bond signal can be observed from the P<sub>red</sub>@CNF sample. The thermogravimetric analysis (TGA) results of each three bunches of samples (before and after the flash-heat treatment) were exhibited in Supplementary Fig. 4, showing good repeatability of the designed synthesis. The weight percentage of the P<sub>red</sub> in the P<sub>red</sub>@CNF composite is ~35%.

## In situ TEM experiments and chemo-mechanical simulation.

Real-time observation of the sodiation process is critical to investigate the electrochemical reaction mechanisms. The architectural core-shell nanostructure ensures the electronic conductivity of the composite in the TEM electrochemical cell, and the one-dimensional space confined by the CNF shell eases the observation and measurement, at the same time. A dry-format electrochemical cell setup was employed for the in situ study of the sodiation<sup>25–27</sup>, as illustrated in Fig. 2a, where the P<sub>red</sub>@CNF composite and Na metal works as the working and counter electrodes, and the native Na<sub>2</sub>O coating formed on Na metal surface serves as the solid-state electrolyte. The cropped time-lapse STEM image series are exhibited in Fig. 2b and Supplementary Movie 1, where the sodiation of four P<sub>red</sub> segments inside a single CNF started almost spontaneously, indicative of the fast sodium-ion conduction through CNF shells. The sodiation process was accomplished within 400 s, demonstrating the good sodiation rate boosted by the P<sub>red</sub>@CNF composite

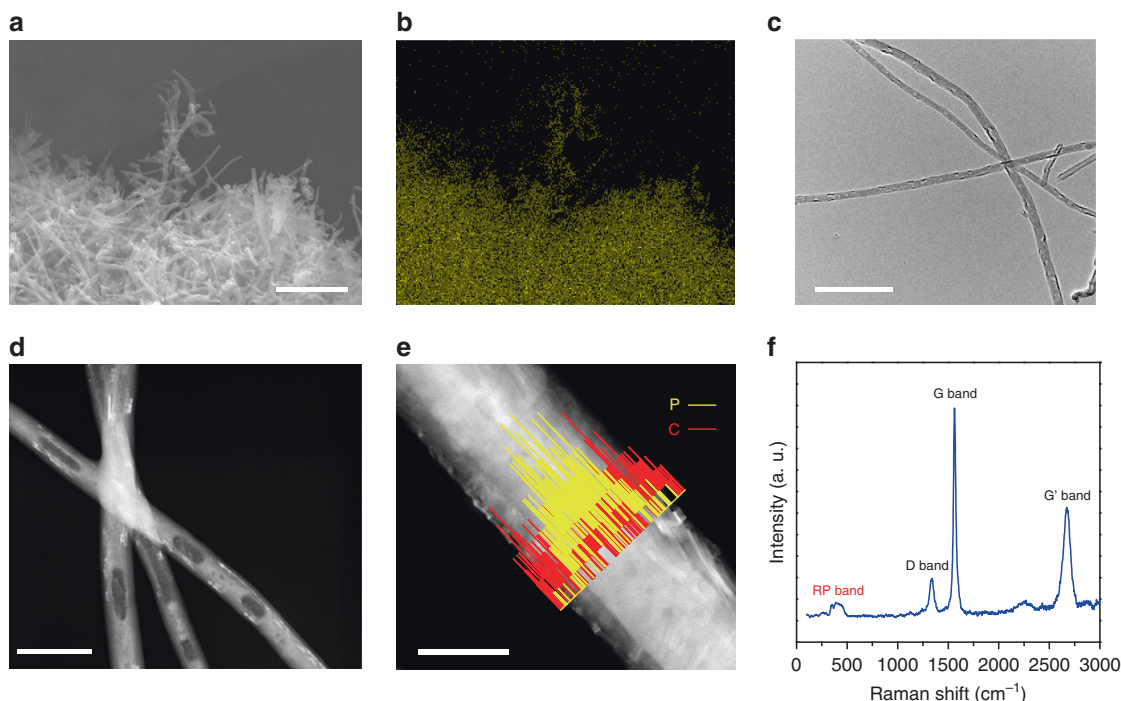


**Fig. 1** Characterization of as-synthesized  $P_{red}@CNF$  composite. **a** SEM image of the  $P_{red}@CNF$  composite. Scale bar is 1  $\mu m$ . **b** EDS elemental map of the phosphorus concentration in **a**. **c**, **d** TEM and STEM images of the  $P_{red}@CNF$  composite. Scale bars are 500 nm and 200 nm for **c** and **d**, respectively. **e** EDS line-scan profiles of phosphorus and carbon. Scale bar is 100 nm. **f** Raman spectra of the as-synthesized  $P_{red}@CNF$  composite.

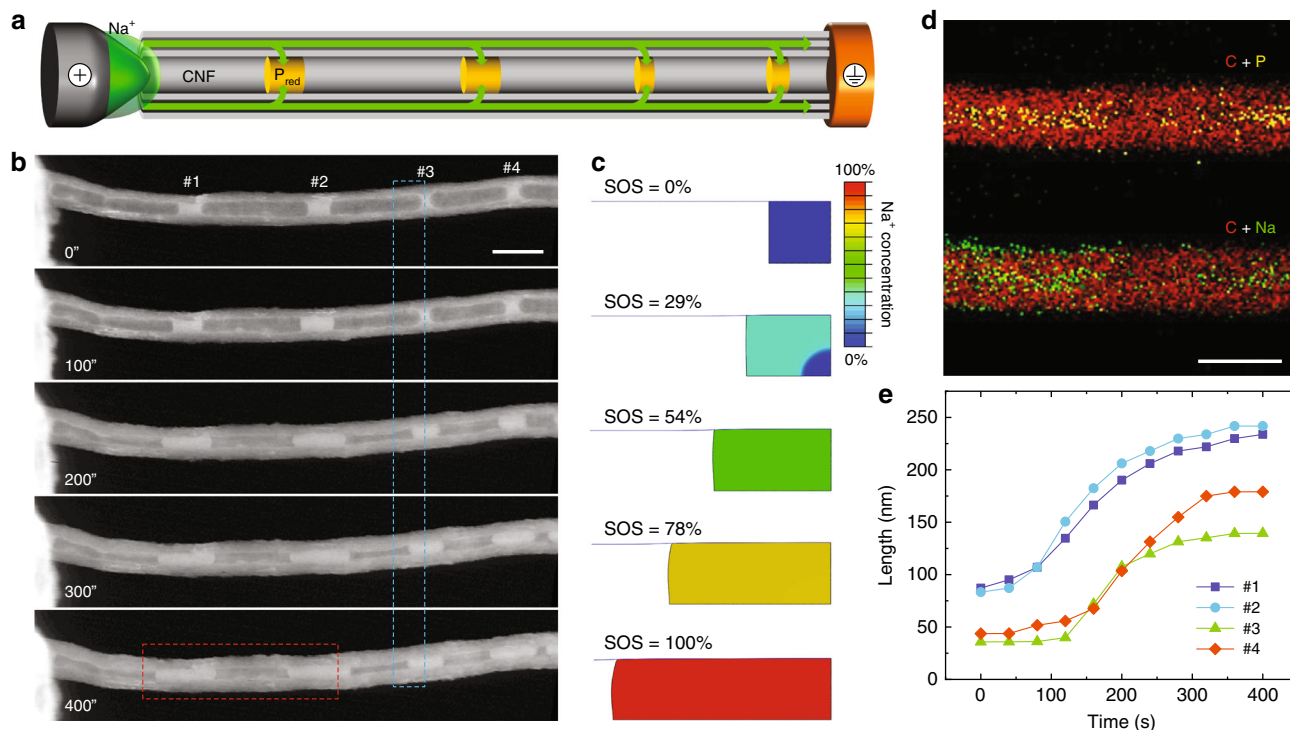


**Fig. 2** In situ TEM experiment with the relevant analysis. **a** Schematic diagram showing the in situ TEM experimental setup of a dry electrochemical cell. **b** STEM image series captured in real-time showing  $P_{red}$  volume expansion during sodiation. Scale bar is 200 nm. **c** Simulated SOS according to the  $P_{red}$  morphological evolution of the region labelled with the blue rectangle in **b**. **d** EDS maps of phosphorus (green), sodium (yellow), and carbon (red) elements of the region labelled with the red rectangle in **b**. Scale bar is 200 nm. **e** The length change of four  $P_{red}$  segments marked in **b** as the function of time during the sodiation process.

architecture. The  $P_{\text{red}}$  segments accommodate the large volume expansion by longitudinal expansion along the inner space of CNF, without causing apparent deformation or cracking of the stiff CNF shell. The drastic extension of  $P_{\text{red}}$  segments shown in Fig. 2b reveals a “liquid-like” material behaviour of  $P_{\text{red}}$  under sodiation: as sodiation advances,  $P_{\text{red}}$  may yield at low yielding stress and exhibit decreasing stiffness (i.e., softening), enabling the  $P_{\text{red}}$  to flow plastically within the CNF as the fluid does. It is worth noting that the observed “liquefaction” phenomena are from the intrinsic nature of  $P_{\text{red}}$ , but not due to the electron beam-induced heating effect<sup>28,29</sup>, which was not observed in other allotropes, such as  $P_{\text{black}}$  (ref. 30). No obvious sodiation reaction front or phase boundary was observed in the experiment. The morphology evolution of  $P_{\text{red}}$  segments with mechanical softening behaviour was modelled as a two-step process via finite element package ABAQUS<sup>31–35</sup>. We defined the state of sodiation (SOS) with SOS = 0% being the pristine unsodiated state and SOS = 100% the fully sodiated state of the  $P_{\text{red}}$ . Simulated  $P_{\text{red}}$  morphologies corresponding to SOS of 0%, 29%, 54%, 78%, and 100% are presented in Fig. 2c, which is in a good agreement with the longitudinal flow of  $P_{\text{red}}$  segments observed in the in situ TEM experiments (for example, see segment #3 in Fig. 2b for comparison, as marked with the blue rectangle). Moreover, the formation of rounded convex edges of  $P_{\text{red}}$  during sodiation is captured by in situ STEM imaging and reproduced by our modelling, indicative of the mechanical interaction between the  $P_{\text{red}}$  segment and CNF. In the simulation results of Supplementary Fig. 5, it is also predicted that a hard  $P_{\text{red}}$  segment without sodiation-induced mechanical softening can deform the CNF in the radial direction significantly, and does not flow as readily as

observed in the experiments, indicative of the softening effect on  $P_{\text{red}}$  from another perspective. The EDS elemental mapping profiles of carbon, sodium, and phosphorus elements are displayed in Fig. 2d, in which the distribution of sodium and phosphorus inside the CNF hollows reached a good agreement, indicative of a complete sodiation process forming sodium phosphides. The substantial volume expansion analysis of the  $P_{\text{red}}$  segments is exhibited in Fig. 2e, where an average longitudinal expansion along CNF of ~330% was confirmed.

Intriguingly, in another set of the cropped time-lapse STEM images depicted in Fig. 3a and Supplementary Movie 2, just like two liquid droplets, two  $P_{\text{red}}$  segments deformed and merged during the sodiation expansion, which confirms the sodiation-induced softening effect of  $P_{\text{red}}$ . Usually,  $P_{\text{red}}$  with polymeric structure can be considered as an intermediate phase between  $P_{\text{white}}$  (soft and waxy due to the molecular structure, and reactive because of the high angular strain of the molecule) and violet phosphorus ( $P_{\text{violet}}$ , stable due to the monoclinic structure). In this approach, considering that the vaporization–condensation synthesized  $P_{\text{red}}$  has relatively weak molecular interactions and loose crystal structure, the sodiation-induced bond breaking may partially convert polymeric  $P_{\text{red}}$  into intermediate phases with similar properties to the soft and waxy  $P_{\text{white}}$ , and introduce the lubricating and softening effects with the “liquid-like” mechanical property.

The modelling results further reveal the mechanical constraint effect provided by the CNF on the stress mitigation in the  $P_{\text{red}}$  during sodiation. Tensile stress on the material surface is the major driving force for electrode fracture and capacity fading during electrochemical cycling. For example, it is the tensile hoop

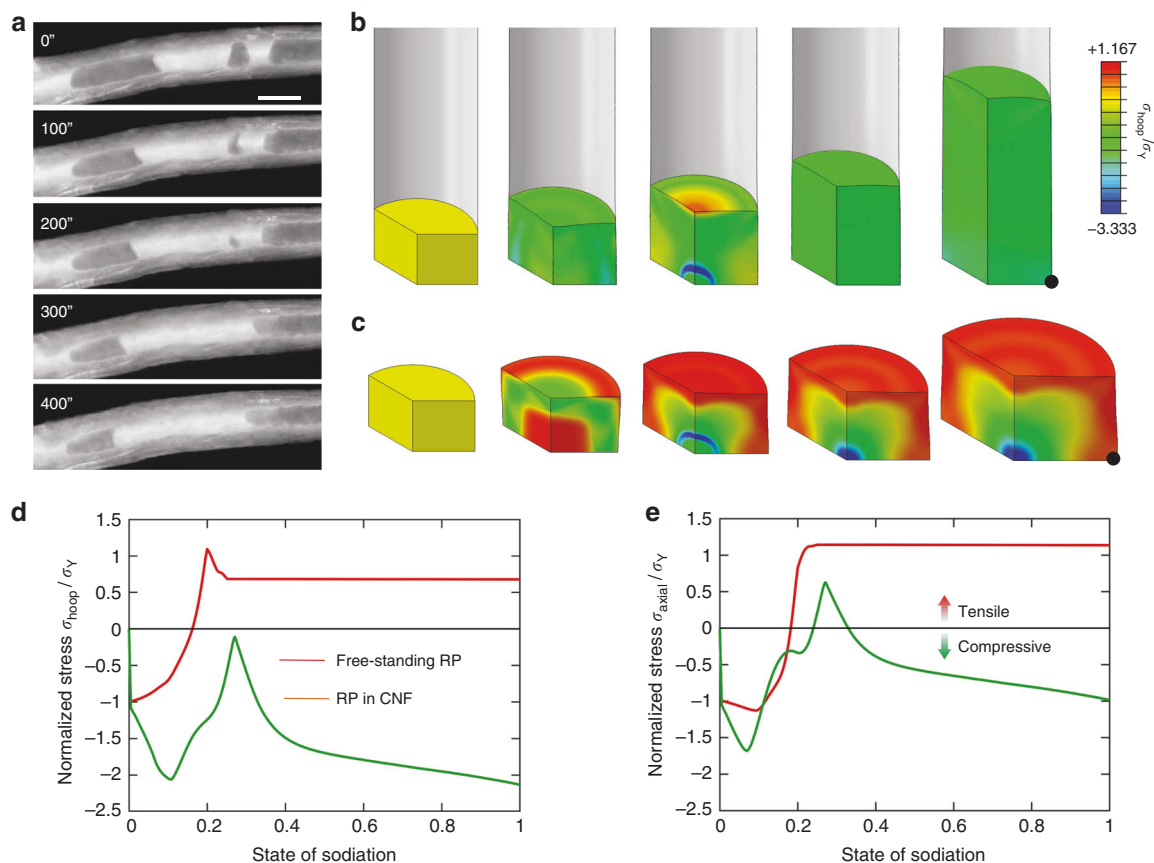


**Fig. 3** “Liquefaction” phenomena with the relevant simulation analysis. **a** STEM image series captured in real-time showing two  $P_{\text{red}}$  segments merging together during sodiation. Scale bar is 100 nm. Simulated hoop stress distribution of **b**  $P_{\text{red}}$ @CNF and **c** a freestanding  $P_{\text{red}}$  particle. **d** Hoop stress evolution and **e** axial stress evolution at the hot spot (labelled by black) of  $P_{\text{red}}$ @CNF and a freestanding  $P_{\text{red}}$  particle during sodiation.

stress (the normal stress in the circumferential direction, Supplementary Fig. 6a) that causes the fracture of nanoparticle and silicon nanowire anodes in lithium-ion batteries. Fig. 3b shows the evolution of hoop stress as well as the morphology of a  $P_{\text{red}}$  segment encapsulated by a CNF shell, with the stress level denoted by the colour contour. The lateral expansion of the  $P_{\text{red}}$  segment is strongly confined by the stiff CNF (Supplementary Fig. 7a–d), driving the  $P_{\text{red}}$  to plastically flow along the longitudinal direction of the CNF. Consequently, the resulting stresses in the CNF-enclosed  $P_{\text{red}}$  segment are largely compressive, which prevents crack initiation in the  $P_{\text{red}}$  segments. As illustrated in Fig. 3c, in contrast to the CNF-encapsulated  $P_{\text{red}}$  segment, higher tensile stresses are apparent near the segment surface of a freestanding  $P_{\text{red}}$  segment, largely due to the pushing-out effect during sodiation and, most importantly, the absence of the mechanical constraint provided by the CNF shell. As evident in Fig. 3d, hoop stress at a hot spot (labelled by the black dot in Fig. 3b, c) on the  $P_{\text{red}}$  segment surface remains compressive during the sodiation process, which is in stark contrast to the high tensile stress developed at the hot spot in the segment without any confinement. The CNF shell not only reduces the hoop stresses in the segment, but also plays an important role in mitigating the axial stresses (the stress in the longitudinal direction, as illustrated in Supplementary Fig. 6b). As revealed in Fig. 3e and Supplementary Fig. 6c, the axial stress on the same hot spot is largely compressive in the CNF-encapsulated  $P_{\text{red}}$  segment during sodiation, while the freestanding segment constantly undergoes tensile axial stress that may cause fracture and capacity fading (Supplementary Fig. 6d). Based on the analysis above, the structural integrity of the  $P_{\text{red}}$  segment can be preserved by the designed strategy, which is beneficial for the cycling stability.

**Electrochemical tests.** The synthesized  $P_{\text{red}}@CNF$  composite was fabricated into freestanding films through vacuum filtration, without any polymer binder or conductive additives, as shown in the optical image of a pouched film electrode presented in Supplementary Fig. 8. The electrochemical performance of the  $P_{\text{red}}@CNF$  anodes was examined in half-type coin cells with sodium metal as counter electrodes.  $NaPF_6$  ( $1.0 \text{ mol L}^{-1}$ ) in an ethylene carbonate (EC)–diethyl carbonate (DEC) solution with fluoroethylene carbonate (FEC) additive (10% by volume) was employed as the electrolyte. Because no obvious P–C bond signals were observed in Raman and XPS results, the specific capacity and current density values are calculated from the mass of phosphorus only.

The cycling stability tests of our  $P_{\text{red}}@CNF$  anodes were performed using galvanostatic charge and discharge with a voltage window of 0.01–2.0 V at 0.1, 0.2, 0.5 and  $1 \text{ A g}^{-1}$  current densities, with cycle numbers up to 522, 1000, 2284, and 5000, as exhibited in Fig. 4a (1–5000 cycles) and 4b (1–500 cycles) marked with different colours, respectively. The Coulombic efficiency at  $1 \text{ A g}^{-1}$  current density is presented as hollow circles against the right axis, and efficiencies at other current densities are plotted in Supplementary Fig. 9. In order to form stable solid electrolyte interface (SEI) films with FEC additive, all four anodes were cycled at  $0.1 \text{ A g}^{-1}$  current density for the first three cycles, as marked with the blue rectangle in Fig. 4b. At  $0.1 \text{ A g}^{-1}$  current rate, the  $P_{\text{red}}@CNF$  anode presents initial specific charge capacities of 2464.5, 2356.8, and  $2275.4 \text{ mAh g}^{-1}$  for the first three cycles, and then the capacity decreased from 2177.3 to  $1862.5 \text{ mAh g}^{-1}$  from the 4th to 522nd cycle with a decay rate of  $\sim 0.03\%$  per cycle. The other three anodes also present excellent capacity retention during long cycling: 2032.3 to  $1721.1 \text{ mAh g}^{-1}$  from the 4th to 991st cycle at  $0.2 \text{ A g}^{-1}$  current density, 1961.6 to  $1361.2 \text{ mAh g}^{-1}$  from the 4th to 2284th cycle at

$0.5 \text{ A g}^{-1}$ , and 1522.4 to  $1019.5 \text{ mAh g}^{-1}$  from the 4th to 5000th cycle at  $1 \text{ A g}^{-1}$ . The superior long cycling performance of  $P_{\text{red}}@CNF$  anode not only confirms that the capacity degradation of  $P_{\text{red}}$  anode mainly comes from the side reactions occurring at the electrode/electrolyte interfaces, but also suggests that our encapsulation strategy is crucial to optimize the electrochemical stability of  $P_{\text{red}}$  anode in sodium-ion chemistry.

The representative voltage potential profiles of the cycling stability test at the current density of  $0.1 \text{ A g}^{-1}$  are exhibited in Fig. 4c, where the cycle numbers are labelled on each curve. Upon the first sodiation process, we observed a major and a minor sodiation plateau at 0.5–0.2 V and 0.7–0.9 V. The minor plateau should be ascribed to the SEI film formation and responsible for the capacity loss at the beginning of the cycling stability tests. The discharge curves display a primary plateau at 0.4–0.2 V for the 2nd, 100th, and 500th cycle, and all charge curves (1st, 2nd, 100th, and 500th cycle) present a primary de-sodiation plateau at 0.4–0.6 V. The voltage potential profiles of the cycling stability tests at other current densities are depicted in Supplementary Fig. 10, in which the hysteresis between charging and discharging curves is slightly enlarged as the current rate increased. The rate performance and the cyclic voltammogram of the  $P_{\text{red}}@CNF$  anode are exhibited in Supplementary Fig. 11 and 12. To investigate the role of SEI film formed with the FEC electrolyte additive, cells with and without FEC were tested at  $0.1 \text{ A g}^{-1}$  current densities, as shown in Supplementary Fig. 13. In contrast to cells without FEC additive, cells with FEC show a less severe capacity degradation and smaller efficiency fluctuation in 100 cycles, signifying that the stable long-term cycling performance necessitates the strong SEI films formed with FEC additive<sup>36–38</sup>.

**Post-cycling characterization.** TEM image of the post-cycling  $P_{\text{red}}@CNF$  anode after 5000 cycles at  $1 \text{ A g}^{-1}$  current density at de-sodiated state (Fig. 4d) shows that the  $P_{\text{red}}$  active material is still confined inside CNFs, indicating that the designed encapsulation strategy with core-shell nanostructure has successfully accommodated the volume variation of  $P_{\text{red}}$  particles, maintained the electronic contact between  $P_{\text{red}}$  cores and CNF shells and suppressed the side reactions consuming  $P_{\text{red}}$  active material. On the other hand, numerous bubbles are found in some of the post-cycling  $P_{\text{red}}@CNF$ . Although the softening effect observed in the in situ TEM experiment (Fig. 3a) could be partially attributed to the heating effect caused by electron beam, bubbles found in the ex situ TEM image (formed by the shrinking of the softened  $P_{\text{red}}$  during the de-sodiation process) further exclude that hypothesis. The intercalation and extraction of alkali metal ions can amorphize anode materials, such as silicon and  $P_{\text{black}}$ <sup>39–41</sup>, and thus the sodiation should be able to break the “chain-like” structure in the polymeric  $P_{\text{red}}$  into intermediate compounds with higher deformability. To investigate the intermediate phases of sodiated  $P_{\text{red}}$ , Raman spectroscopy was performed on five sodiated  $P_{\text{red}}@CNF$  samples, as shown in Supplementary Fig. 14. Realizing the complexity of the P–P covalent structure in phosphorus<sup>42,43</sup>, the in situ Raman spectroscopy is highly preferred here. However, due to the limitation of our equipment, we performed ex situ Raman experiments on the electrochemically sodiated samples by discharging electrodes to 0.05 V at  $1 \text{ A g}^{-1}$  current rate. In contrast to the spectrum of as-synthesized  $P_{\text{red}}@CNF$  in Supplementary Fig. 14b, the  $P_{\text{red}}$  signal intensity of the five sodiated  $P_{\text{red}}@CNF$  samples was greatly reduced in Supplementary Fig. 14a, as marked by the light red colour, indicative of the sodiation-induced P–P bond breaking and the formation of sodiated phosphorus compounds. In Supplementary Fig. 14a, the sodiated samples also presented a new band from 520 to  $620 \text{ cm}^{-1}$  (marked by the light blue colour), indicative of the

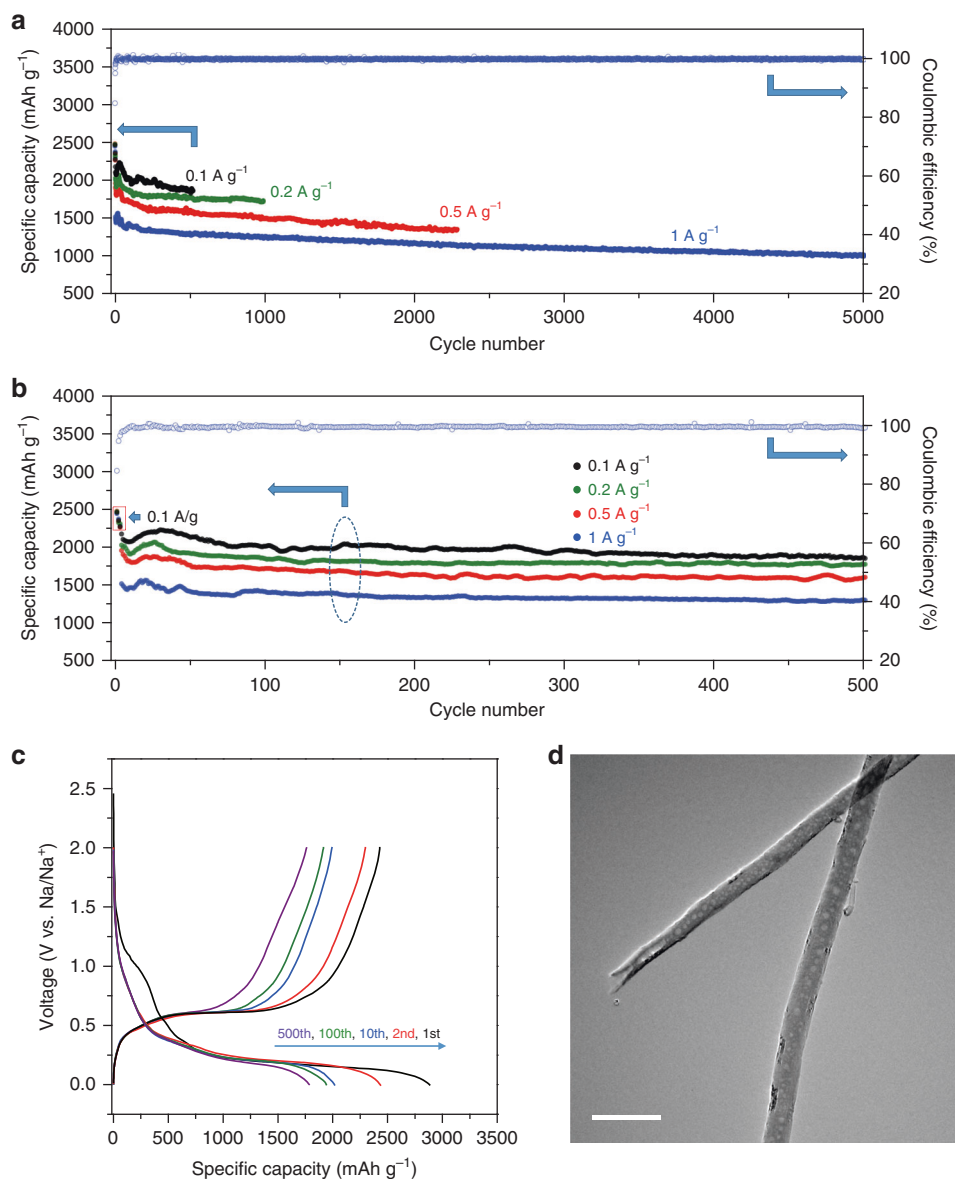


**Fig. 4** Electrochemical cycling performance and post-cycling TEM image. **a, b** Reversible de-sodiation specific capacity of the  $P_{red}@CNF$  anodes at different current densities with cycle numbers up to 5000 and 500. The charge and discharge current densities of four anodes were  $0.1 \text{ A g}^{-1}$  for the first three cycles, and  $0.1$ ,  $0.2$ ,  $0.5$ , and  $1 \text{ A g}^{-1}$  for later cycles marked in black, green, red, and blue, respectively. Each specific de-sodiation capacity data point is presented as a solid dot against the left axis, and Coulombic efficiency at  $1 \text{ A g}^{-1}$  current density is presented as hollow circles against the right axis. **c** Sodiation and de-sodiation potential profiles at  $0.1 \text{ A g}^{-1}$  current density (black curve in **a** and **b**), marked with representative cycle numbers. **d** Post-cycling TEM image of  $P_{red}@CNF$  after 5000 cycles at  $1 \text{ A g}^{-1}$  current density. Scale bar is 200 nm.

intermediate phase formation, given the fact that  $P_{white}$  has characteristic Raman peaks at 367, 462, and  $606 \text{ cm}^{-1}$  <sup>44,45</sup>.

## Discussion

For alloying anodes, such as silicon and tin, large volume variation always accompanies high capacity and high risk of material pulverization; and for silicon materials, a particle size of  $\sim 150 \text{ nm}$  was believed to be the “no-fracture” size during lithiation<sup>46</sup>. Our observation showed that, instead of pulverization, the sodiation could result in the “liquid-like” behaviour of  $P_{red}$  particles, and thus  $P_{red}$  should have a much larger “no-fracture” size for sodium intercalation than that of silicon for lithium. The sodiation-induced softening of  $P_{red}$  reveals the superior malleability and deformability toward mitigating the adverse mechanical effects in an electrochemical battery system. Our study also suggests that, to further improve the electrochemical

performance of  $P_{red}$ -based anodes, part of the efforts should be devoted to the interface engineering at the electrode/electrolyte interfaces to avoid unfavourable side reactions, and the potential explorations could be conformal encapsulation and surface coating, artificial SEI films, and new electrolyte/additive combinations for even stronger SEI films.

## Conclusion

In summary, we investigated the sodiation process of synthesized  $P_{red}$ -impregnated CNF composite through in situ TEM and chemo-mechanical simulation. The results of our study show that  $P_{red}$  particles can be softened during sodiation and thus it gains excellent malleability toward the high-capacity sodium-ion anodes. The fabricated  $P_{red}@CNF$  anodes can deliver  $\sim 1850 \text{ mAh g}^{-1}$  specific charge capacity over 500 cycles at  $0.1 \text{ A g}^{-1}$  current density, and  $>1000 \text{ mAh g}^{-1}$  capacity over 5000

cycles at  $1 \text{ A g}^{-1}$  current rate. The excellent long-term cycling performance proves that the encapsulation strategy designed here can successfully suppress the unfavourable side reactions. Together, our studies provide an avenue to desirable sodium-ion anodes, and we hope that the data reported in this work will stimulate more theoretical and experimental efforts to explore phosphorus-based battery materials.

## Methods

**Materials preparation.** The  $\text{P}_{\text{red}}$  was purchased from Spectrum Chemical Mfg. Corp. with 99.99% purity and the  $\text{P}_{\text{red}}$  powder was heated to  $90^\circ\text{C}$  to remove the moisture. After drying, the powder was meshed in an argon-filled glovebox, using a mesh filter with  $30 \mu\text{m}$  pore size. CNF powder (PR-XT-HHT from Pyrograf Products) was ultrasonicated in ethanol alcohol to break the ultra-long fibres and then annealed in argon flow at  $1000^\circ\text{C}$  for 6 h to remove the moisture and unfavourable functional groups on both inner and outer surface of the CNFs. The  $\text{P}_{\text{red}}$  and CNF powder was mixed and filled into a 10-cm-long one-end-closed quartz tube in the glovebox, and the phosphorus/carbon weight ratio is 5:1. An ampoule was made by sealing the opening of the quartz tube under vacuum. In an argon-flowed tube furnace, the ampoule was heated at  $550^\circ\text{C}$  for 30 min and then maintained at  $280^\circ\text{C}$  overnight to convert existing  $\text{P}_{\text{white}}$  to  $\text{P}_{\text{red}}$ . The ampoule was transferred into glovebox, and the product powder was taken out from the ampoule and transferred into an argon-flowed ( $350 \text{ sccm}$ ) tube furnace for the flash-heat treatment to remove the exceeding  $\text{P}_{\text{red}}$ : the ceramic boat with product powder was first placed at the upstream region out of the heating zone, and then the boat was transferred into the heating zone for a flash-heat treatment at  $600^\circ\text{C}$  for 90 s, and then the boat was maintained at  $280^\circ\text{C}$  overnight with a cooling down process to get the final product. The resulted  $\text{P}_{\text{red}}@\text{CNF}$  composite was assembled to a film through filtration in a glovebox, without any polymer binder or conductive carbon additive, and then the film was punched into discs with a diameter of 14 mm. The punched film discs were employed as electrodes directly in the subsequent electrochemical experiments. The mass of each  $\text{P}_{\text{red}}@\text{CNF}$  film electrode is  $\sim 2.4 \text{ mg}$ , and the loading mass of the  $\text{P}_{\text{red}}$  in each film electrode is  $\sim 0.84 \text{ mg}$  according to the TGA results presented in Supplementary Fig. 4.

**Materials characterization.** We examined surface morphology of synthesized samples using a JEOL 7001F-LV field-emission scanning electron microscope, with EDS module. We collected Raman spectra using a Renishaw inVia Raman Microscope, operating at  $532 \text{ nm}$  wavelength. The ex situ TEM, HAADF-STEM, and EDS element mapping analysis experiments were performed on a JEOL JEM 2100F field-emission (TEM), operating at  $200 \text{ kV}$ . In the ex situ TEM observation, synthesized sample powder was uniformly dispersed in solvents, such as ethanol, and then the mixture solution was dropped onto TEM grids (carbon-film-covered copper grids) and dried in an argon-filled glovebox. TGA was performed under a nitrogen atmosphere with a heating rate of  $1^\circ\text{C}$  per minute, using a Netzsch Simultaneous Thermal Analyser.

**In situ TEM experiments.** The in situ TEM electrochemical cell was incorporated into a Nanofactory TEM-STM specimen holder, in which the  $\text{P}_{\text{red}}@\text{CNF}$  composite was dispersed onto a TEM half-grid with amorphous carbon support, as the active electrode material and current collector. Na metal was attached to a tungsten probe as the counter electrode, where a native  $\text{Na}_2\text{O}$  layer formed on Na metal was employed as the solid electrolyte. Materials were assembled onto the specimen holder in an argon-filled glovebox, and then the assembly was transferred to the electron microscope using a sealed argon bag to prevent air exposure. The sodiation processes were recorded in real-time under TEM or STEM mode, using a TEM (JEOL 2100F), operating at  $200 \text{ kV}$ .

**Chemo-mechanical simulation.** Considering the similarity between  $\text{P}_{\text{red}}$ , amorphous silicon, and germanium, we simulate the sodiation of the  $\text{P}_{\text{red}}$  segment by a phenomenological two-step two-phase model. The sodiation is modelled by a nonlinear diffusion of Na with a diffusivity of  $D = D_0[C_0/(C_0 - C) - 4C]$ , where  $D_0$  is a diffusivity constant,  $C$  is the normalized Na concentration, and  $C_0$  is the local Na concentration required to break P-P bonds, and thus specifies the Na concentration of the intermediate phase during the two-step sodiation. Note that here the Na concentration is normalized by that of the fully sodiated phase  $\text{Na}_3\text{P}$ ; namely,  $C$  is zero represents pure phosphorus, while  $C$  is one represents  $\text{Na}_3\text{P}$ . To illustrate the sodiation-induced deformation, an elastic and perfectly plastic model is adopted, with the total strain rate being a sum of three parts:  $\dot{\epsilon}_{ij} = \dot{\epsilon}_{ij}^e + \dot{\epsilon}_{ij}^p + \dot{\epsilon}_{ij}^v$  ( $i = 1, 2, 3$  and  $j = 1, 2, 3$ ). Here  $\dot{\epsilon}_{ij}^e$  and  $\dot{\epsilon}_{ij}^p$  present the elastic and plastic strain rate, respectively;  $\dot{\epsilon}_{ij}^v$  presents the sodiation-induced volumetric strain rate and is related to the rate of normalized Na concentration  $\dot{C}$  by  $\dot{\epsilon}_{ij}^v = \beta_{ij}\dot{C}$ , where  $\beta_{ij}$  is the volume expansion coefficient caused by sodiation. The above nonlinear diffusion and elastic perfectly plastic model is numerically implemented in the finite element package ABAQUS to investigate the sodiation of  $\text{P}_{\text{red}}$  segments. In finite-element-based chemo-mechanical simulations, we take advantage of the axis-symmetric

nature of the structure to reduce the numerical expanse. A CNF-encapsulated  $\text{P}_{\text{red}}$  segment is initially pristine and subjected to a constant Na flux  $I_0$  at its surface. The intermediate concentration  $C_0$  is set to be 0.3, considering the fact that P-P bond in  $\text{P}_{\text{red}}$  is weaker than Si-Si bonds in amorphous silicon (which corresponds to  $C_0 = 0.67$ ). The volume expansion coefficient  $\beta_{ij}$  ( $i = 1, 2, 3$  and  $j = 1, 2, 3$ ) is taken to be 0.462 to give a total volume increase of 300% at the formation of  $\text{Na}_3\text{P}$  (note that the true volumetric strain is 0.462 at full sodiation and the associated engineering strain is 0.587). The yield stress  $\sigma_Y = 0.03E$ , where Young's modulus  $E$  is taken to be  $10 \text{ MPa}$  for sodiated  $\text{P}_{\text{red}}$ , and Poisson's ratio  $\nu = 0.3$ . The CNF is modelled by shell elements with Young's modulus of  $50 \text{ GPa}$  and Poisson's ratio of 0.3. The mechanical interaction between the  $\text{P}_{\text{red}}$  segment and the CNF inner surface is described by a hard contact behaviour with a friction coefficient of 0.07.

**Electrochemical measurements.** Using the  $\text{P}_{\text{red}}@\text{CNF}$  film as working electrodes, all electrochemical measurements were carried out in half cells (CR2032-type coin cell) with sodium metal foils as counter electrodes, and  $1.0 \text{ mol L}^{-1}$   $\text{NaPF}_6$  (Sigma-Aldrich, >99%) was mixed with EC-DEC as the electrolyte. Targeting a LiF-enriched SEI film with good electrochemical and mechanical stability, FEC was added into the electrolyte (10%, by volume) as additive. Before assembling electrodes into coin cells, all electrodes were fully immersed in electrolyte overnight (at least 12 h). All cells were assembled inside an argon-filled glovebox. Battery cells were tested with the voltage window of  $0.01\text{--}1.5 \text{ V}$  vs.  $\text{Na}/\text{Na}^+$ . In order to optimize the cycling performance, for the first three cycles, anodes were cycling at  $0.1 \text{ A g}^{-1}$  current density to form stable SEI layers at the earliest stage of the cycling test. All of the capacity and current density volumes were calculated from the mass of phosphorus only. For the ex situ Raman experiments, the as-prepared  $\text{P}_{\text{red}}@\text{CNF}$  film electrodes were assembled into battery cells and discharged to  $0.05 \text{ V}$  at  $1 \text{ A g}^{-1}$  current rate. The sodiated electrodes were taken out from the disassembled cells and washed with electrolyte solvent briefly in a glovebox, and then sealed between two glass slides for Raman spectroscopy investigation.

## Data availability

All data generated in this study and supported the findings of this work are available from the corresponding author on reasonable request.

## Code availability

The code employed in this study and supported the findings of this study are available from the corresponding author on reasonable request.

Received: 11 June 2019; Accepted: 17 March 2020;

Published online: 20 May 2020

## References

- Bruce, P. G., Scrosati, B. & Tarascon, J.-M. Nanomaterials for rechargeable lithium batteries. *Angew. Chem. Int. Ed.* **47**, 2930–2946 (2008).
- Arico, A. S., Bruce, P., Scrosati, B., Tarascon, J.-M. & van Schalkwijk, W. Nanostructured materials for advanced energy conversion and storage devices. *Nat. Mater.* **4**, 366–377 (2005).
- Kasavajula, U., Wang, C. & Appleby, A. J. Nano- and bulk-silicon-based insertion anodes for lithium-ion secondary cells. *J. Power Sources* **163**, 1003–1039 (2007).
- Dunn, B., Kamath, H. & Tarascon, J.-M. Electrical energy storage for the grid: a battery of choices. *Science* **334**, 928–935 (2011).
- Luo, W. et al. Na-ion battery anodes: materials and electrochemistry. *Acc. Chem. Res.* **49**, 231–240 (2016).
- Liu, Y., Merinov, B. V. & Goddard, W. A. Origin of low sodium capacity in graphite and generally weak substrate binding of Na and Mg among alkali and alkaline earth metals. *Proc. Natl Acad. Sci. USA* **113**, 3735–3739 (2016).
- Yang, F., Gao, H., Chen, J. & Guo, Z. Phosphorus-based materials as the anode for sodium-ion batteries. *Small Methods* **1**, 1700216 (2017).
- Xu, G.-L. et al. Challenges in developing electrodes, electrolytes, and diagnostics tools to understand and advance sodium-ion batteries. *Adv. Energy Mater.* **8**, 1702403 (2018).
- Qian, J., Wu, X., Cao, Y., Ai, X. & Yang, H. High capacity and rate capability of amorphous phosphorus for sodium ion batteries. *Angew. Chem. Int. Ed.* **52**, 4633–4636 (2013).
- Huang, Z. et al. Layer-tunable phosphorene doped by the cation insertion rate as a sodium-storage anode. *Adv. Mater.* **29**, 1702372 (2017).
- Li, W.-J., Chou, S.-L., Wang, J.-Z., Liu, H.-K. & Dou, S.-X. Simply mixed commercial red phosphorus and carbon nanotube composite with exceptionally reversible sodium-ion storage. *Nano Lett.* **13**, 5480–5484 (2013).
- Zhu, Y. et al. Red phosphorus-single-walled carbon nanotube composite as a superior anode for sodium ion batteries. *ACS Nano* **9**, 3254–3264 (2015).

13. Song, J. et al. Advanced sodium ion battery anode constructed via chemical bonding between phosphorus, carbon nanotube, and cross-linked polymer binder. *ACS Nano* **9**, 11933–11941 (2015).
14. Song, J. et al. Chemically bonded phosphorus/graphene hybrid as a high performance anode for sodium-ion batteries. *Nano Lett.* **14**, 6329–6335 (2014).
15. Zhang, C. et al. Amorphous phosphorus/nitrogen-doped graphene paper for ultrastable sodium-ion batteries. *Nano Lett.* **16**, 2054–2060 (2016).
16. Liu, Y. et al. Red phosphorus nanodots on reduced graphene oxide as a flexible and ultra-fast anode for sodium-ion batteries. *ACS Nano* **11**, 5530–5537 (2017).
17. Kim, Y. et al. An amorphous red phosphorus/carbon composite as a promising anode material for sodium ion batteries. *Adv. Mater.* **25**, 3045–3049 (2013).
18. Sun, J. et al. Carbothermic reduction synthesis of red phosphorus-filled 3D carbon material as a high-capacity anode for sodium ion batteries. *Energy Storage Mater.* **4**, 130–136 (2016).
19. Li, W. et al. Amorphous red phosphorus embedded in highly ordered mesoporous carbon with superior lithium and sodium storage capacity. *Nano Lett.* **16**, 1546–1553 (2016).
20. Li, W. et al. Confined amorphous red phosphorus in MOF-derived N-doped microporous carbon as a superior anode for sodium-ion battery. *Adv. Mater.* **29**, 1605820 (2017).
21. Hou, H. et al. Carbon quantum dots and their derivative 3D porous carbon frameworks for sodium-ion batteries with ultralong cycle life. *Adv. Mater.* **27**, 7861–7866 (2015).
22. Boskovic, B. O., Stolojan, V., Khan, R. U. A., Haq, S. & Silva, S. R. P. Large-area synthesis of carbon nanofibres at room temperature. *Nat. Mater.* **1**, 165–168 (2002).
23. Fantini, C. et al. Optical transition energies for carbon nanotubes from resonant Raman spectroscopy: environment and temperature effects. *Phys. Rev. Lett.* **93**, 147406 (2004).
24. Sun, J. et al. Formation of stable phosphorus-carbon bond for enhanced performance in black phosphorus nanoparticle-graphite composite battery anodes. *Nano Lett.* **14**, 4573–4580 (2014).
25. He, K. et al. Visualizing nonequilibrium lithiation of spinel oxide via in situ transmission electron microscopy. *Nat. Commun.* **7**, 11441 (2016).
26. Gu, M. et al. Probing the failure mechanism of SnO<sub>2</sub> nanowires for sodium-ion batteries. *Nano Lett.* **13**, 5203–5211 (2013).
27. Yuan, Y., Amine, K., Lu, J. & Shahbazian-Yassar, R. Understanding materials challenges for rechargeable ion batteries with in situ transmission electron microscopy. *Nat. Commun.* **8**, 15806 (2017).
28. Egerton, R. F., Li, P. & Malac, M. Radiation damage in the TEM and SEM. *Micron* **35**, 399–409 (2004).
29. Egerton, R. F. Control of radiation damage in the TEM. *Ultramicroscopy* **127**, 100–108 (2013).
30. Kim, S., Cui, J., Dravid, V. P. & He, K. Orientation-dependent intercalation channels for lithium and sodium in black phosphorus. *Adv. Mater.* **31**, 1904623 (2019).
31. Jia, Z. & Li, T. Intrinsic stress mitigation via elastic softening during two-step electrochemical lithiation of amorphous silicon. *J. Mech. Phys. Solids* **91**, 278–290 (2016).
32. Wang, J. W. et al. Two-phase electrochemical lithiation in amorphous silicon. *Nano Lett.* **13**, 709–715 (2013).
33. Wang, J. W., Liu, X. H., Mao, S. X. & Huang, J. Y. Microstructural evolution of tin nanoparticles during in situ sodium insertion and extraction. *Nano Lett.* **12**, 5897–5902 (2012).
34. Liang, W. et al. Tough germanium nanoparticles under electrochemical cycling. *ACS Nano* **7**, 3427–3433 (2013).
35. Wang, J. et al. Structural evolution and pulverization of tin nanoparticles during lithiation-delithiation cycling. *J. Electrochem. Soc.* **161**, F3019–F3024 (2014).
36. Xu, K. Electrolytes and interphases in Li-ion batteries and beyond. *Chem. Rev.* **114**, 11503–11618 (2014).
37. Komaba, S. et al. Fluorinated ethylene carbonate as electrolyte additive for rechargeable Na batteries. *ACS Appl. Mater. Interfaces* **3**, 4165–4168 (2011).
38. Schroder, K. et al. The effect of fluoroethylene carbonate as an additive on the solid electrolyte interphase on silicon lithium-ion electrodes. *Chem. Mater.* **27**, 5531–5542 (2015).
39. Obrovac, M. N. & Christensen, L. Structural changes in silicon anodes during lithium insertion/extraction. *Electrochem. Solid-State Lett.* **7**, A93–A96 (2004).
40. Hembram, K. P. S. S. et al. Unraveling the atomistic sodiation mechanism of black phosphorus for sodium ion batteries by first-principles calculations. *J. Phys. Chem. C* **119**, 15041–15046 (2015).
41. Liu, Y. et al. Room-temperature pressure synthesis of layered black phosphorus-graphene composite for sodium-ion battery anodes. *ACS Nano* **12**, 8323–8329 (2018).
42. Böcker, S. & Häse, M. Covalent structures of phosphorus: a comprehensive theoretical study. *Z. Anorg. Allg. Chem.* **621**, 258–286 (1995).
43. Häse, M. Structural rules of phosphorus. *J. Am. Chem. Soc.* **116**, 6925–6926 (1994).
44. Brassington, N. J., Edwards, H. G. M. & Long, D. A. The vibration-rotation Raman spectrum of P<sub>4</sub>. *J. Raman Spectrosc.* **11**, 346–348 (1981).
45. Hart, M. et al. Encapsulation and polymerization of white phosphorus inside single-wall carbon nanotubes. *Angew. Chem. Int. Ed.* **56**, 8144–8148 (2017).
46. Liu, X. H. et al. Size-dependent fracture of silicon nanoparticles during lithiation. *ACS Nano* **6**, 1522–1531 (2012).

## Acknowledgements

Data and/or images presented in this study were collected at the Core Center of Excellence in Nano Imaging at the University of Southern California. Y. L., Q. L., M. C., and C. Z. acknowledge National Science Foundation for financial support under Grant 769K521. We would like to acknowledge the financial aid of this research with King Abdul-Aziz City for Science and Technology (KACST) via The center of Excellence for Nanotechnologies (CEGN). K.H. acknowledges Clemson University's start-up fund and CU-CIA grant for use of Electron Microscopy Facility, which was funded in part by Clemson University's R-Initiative Program. Z.J. is grateful for the support of National Natural Science Foundation of China (grant number: 11802269). We thank Prof. Stephen Burke Cronin for access to the Raman facility, and we also thank Bingya Hou, Haotian Shi, Bo Wang, Bofan Zhao, and Zhi Cai for the help of Raman experiments.

## Author contributions

Y.L., K.H., Z.J., and C.Z. co-designed the research. Y.L. and Q.L. conducted material synthesis, characterization, and electrochemical tests. K.H. conducted the in situ TEM experiments. C.J., T.L., and Z.J. conducted the chemo-mechanical simulation. M.C. and Z.L. contributed to the XPS and TGA measurements. D.C. contributed to the data collection of rate capability, cyclic voltammetry, and FTIR experiments. C.Z. supervised the research. Y.L., Q.L., K.H., Z.J., and C.Z. co-drafted the manuscript. T.N. contributed to the discussion of the “liquefaction” phenomena and mechanism. All authors analyzed and discussed the results, and revised the manuscript.

## Competing interests

The authors declare no competing interests.

## Additional information

Supplementary information is available for this paper at <https://doi.org/10.1038/s41467-020-16077-z>.

Correspondence and requests for materials should be addressed to Y.L., K.H., Z.J. or C.Z.

Peer review information *Nature Communications* thanks the anonymous reviewer(s) for their contribution to the peer review of this work.

Reprints and permission information is available at <http://www.nature.com/reprints>

Publisher's note Springer Nature remains neutral with regard to jurisdictional claims in published maps and institutional affiliations.



**Open Access** This article is licensed under a Creative Commons Attribution 4.0 International License, which permits use, sharing, adaptation, distribution and reproduction in any medium or format, as long as you give appropriate credit to the original author(s) and the source, provide a link to the Creative Commons license, and indicate if changes were made. The images or other third party material in this article are included in the article's Creative Commons license, unless indicated otherwise in a credit line to the material. If material is not included in the article's Creative Commons license and your intended use is not permitted by statutory regulation or exceeds the permitted use, you will need to obtain permission directly from the copyright holder. To view a copy of this license, visit <http://creativecommons.org/licenses/by/4.0/>.

© The Author(s) 2020